nature geoscience

ARTICLES

https://doi.org/10.1038/s41561-019-0359-x

Periodic changes in the Cretaceous ocean and climate caused by marine redox see-saw

Klaus Wallmann[1]*, Sascha Flögel[1], Florian Scholz[1], Andrew W. Dale[1], Tronje P. Kemena[1], Sebastian Steinig[1] and Wolfgang Kuhnt[2]

Periodic changes in sediment composition are usually ascribed to insolation forcing controlled by Earth's orbital parameters. During the Cretaceous Thermal Maximum at 97–91 Myr ago (Ma), a 37–50-kyr-long cycle that is generally believed to reflect obliquity forcing dominates the sediment record. Here, we use a numerical ocean model to show that a cycle of this length can be generated by marine biogeochemical processes without applying orbital forcing. According to our model, the restricted proto-North Atlantic and Tethys basins were poorly ventilated and oscillated between iron-rich and sulfidic (euxinic) states. The Panthalassa Basin was fertilized by dissolved iron originating from the proto-North Atlantic. Hence, it was less oxygenated while the proto-North Atlantic was in an iron-rich state and better oxygenated during euxinic periods in the proto-North Atlantic. This redox see-saw was strong enough to create significant changes in atmospheric p_{CO_2}. We conclude that most of the variability in the mid-Cretaceous ocean–atmosphere system can be ascribed to the internal redox see-saw and its response to external orbital forcing.

The Cretaceous Thermal Maximum is marked by high surface and deep-water temperatures[1,2] and rhythmic marine sedimentation with periodic changes in carbon burial, bottom water oxygenation, $\delta^{13}C$ and carbonate $\delta^{18}O$ (refs. [1,3–6]). This period also includes a prominent Ocean Anoxic Event (OAE2) and has emerged as a model case study for the integration of orbital variability with high-resolution geochemical time-series data[3]. Analysis of sedimentary records from the proto-North Atlantic (NAT)[3–6] and the Western Interior Seaway[7,8] reveals that most of the variability in geochemical data occurs with a cycle length of about 37–50 kyr and might therefore be related to obliquity forcing (axial tilt). Several hypotheses have been advanced to explain how obliquity might affect low-latitude sedimentary records from the mid-Cretaceous ocean despite the influence of this orbital parameter on low-latitude insolation being very small[9]. These include obliquity-induced changes in coastal/equatorial upwelling[10], global ocean circulation[3], continental hydrology and weathering[11,12] and carbon storage in permafrost soils[13,14]. However, none of these ideas has been substantiated and supported by carbon cycle modelling.

Here, we present a new redox-resolving biogeochemical ocean model (REDBIO) that generates the 37–50 kyr cycles observed in the geological record without invoking any of the orbital forcing hypotheses outlined above. In this model, global inventories of nutrients used by phytoplankton (phosphate, nitrate, iron) depend on the oxygenation of intermediate and deep waters. Nitrate is consumed under low-oxygen conditions by pelagic and benthic denitrification[15] whereas the release of dissolved phosphate and iron from sediments is promoted when bottom waters turn anoxic[16–18]. Sulfide accumulation in the water column is caused by pelagic and benthic sulfate reduction, and induces pyrite formation and a decline in benthic iron release[19,20]. In a mid-Cretaceous continent–ocean configuration with a poorly ventilated NAT and Tethys, feedbacks between ocean productivity, respiration and benthic nutrient release create self-sustained oscillations with 37–50 kyr cycles in ocean productivity, seawater redox, $\delta^{13}C$ and organic carbon accumulation. These periodic changes are not a predefined model feature but emerge as a result of biogeochemical feedbacks over a significant portion of the model parameter space. Changes in marine export production (EP) created by these cycles are strong enough to induce changes in the atmospheric partial pressure of CO_2 (p_{CO_2}) and global climate.

The marine redox see-saw

A University of Victoria (UVic) Earth system model with a mid-Cretaceous continent configuration was set up and run to steady state over a range of p_{CO_2} values. A comprehensive description of the UVic model is given in the Supplementary Information (Supplementary Section 1, Supplementary Figs. 1–7). The UVic simulations yield dissolved oxygen distributions at intermediate water depths (Supplementary Fig. 5) that are largely consistent with the proxy record (Supplementary Fig. 6) and previous model results for the Cretaceous Thermal Maximum[21,22]. Intermediate waters are oxygen-depleted at low latitudes in the NAT, Tethys and Eastern Equatorial Panthalassa, and are better ventilated at higher latitudes and in most of the Panthalassa Ocean[21,23]. Dissolved oxygen concentrations decline with increasing p_{CO_2} as oxygen solubility is diminished by the concomitant rise in sea surface temperatures (Supplementary Fig. 7). The numerical costs of the UVic model are too high to simulate the evolution of the dynamic phosphate inventory on orbital timescales. A box model (REDBIO) was therefore derived from UVic model outputs (annual mean water fluxes and temperatures) to study how variable P inputs and dynamic phosphate inventories may affect ocean productivity and oxygenation (Supplementary Fig. 8). REDBIO was integrated until a new steady state was attained by applying a constant p_{CO_2} of 500 ppm and a range of riverine phosphorus fluxes (Fig. 1) that correspond to phosphate residence times of 13–29 kyr (global marine P inventory/riverine P flux)[17,24]. Steady-state EP increases with riverine P input while oxygen concentrations in intermediate and deep waters decline due to the concomitant rise in respiration[21,25]. At intermediate riverine P fluxes (107–125 Gmol yr^{-1}), which result in

[1]GEOMAR Helmholtz Centre for Ocean Research Kiel, Kiel, Germany. [2]Institut für Geowissenschaften, University of Kiel, Kiel, Germany.
*e-mail: kwallmann@geomar.de

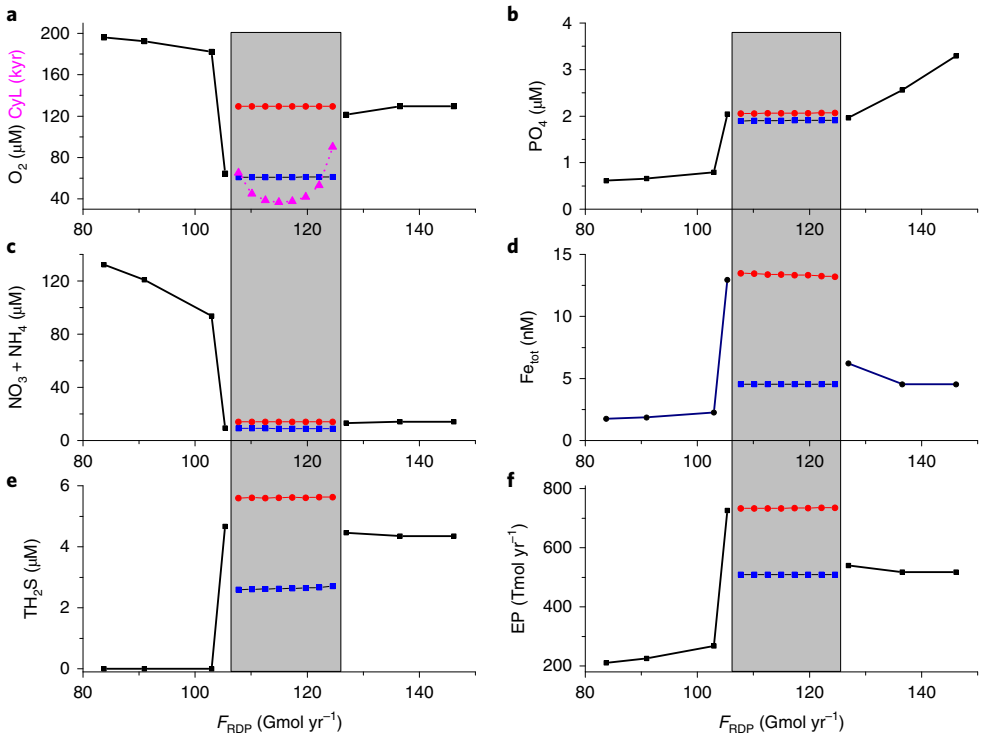

Fig. 1 | Response of the REDBIO model to changes in the riverine P flux. a–f, Global mean concentrations (**a**–**e**) and global EP (**f**) attained after a simulation period of 500 kyr at constant p_{CO_2}(500 ppm) for a range of riverine phosphorus fluxes (F_{RDP}). The grey shading indicates the region where REDBIO does not converge to a steady state, but instead generates regular oscillations (107–125 Gmol yr^{-1}). The minimum and peak values attained over these cycles are indicated as blue squares and red dots, respectively. **a**, Dissolved oxygen concentration and cycle length of the oscillation (CyL). **b**, Dissolved phosphate concentrations. **c**, Dissolved reactive nitrogen concentrations (the sum of nitrate and ammonium). **d**, Dissolved iron concentration (Fe_{tot}, the sum of ferrous and ferric iron). **e**, Total dissolved sulfide concentrations. **f**, EP of POC at 240 m water depth.

global mean phosphate concentrations close to 2 μM, an interesting behaviour emerges. Under these conditions, the model does not converge to a steady state but generates regular oscillations in ocean oxygenation and productivity with constant amplitudes but variable cycle lengths centred at about 40 kyr (Fig. 1).

This internal oscillation is driven by redox transitions in the NAT (Fig. 2). According to the REDBIO model, this poorly ventilated basin oscillates between a state in which intermediate waters are enriched in dissolved iron released from reducing sediments[18,19], and an euxinic state[26] in which dissolved sulfide accumulates in intermediate waters and benthic iron fluxes are diminished by sedimentary pyrite precipitation[20]. The ratio between pyrite-bound iron (Fe_{Py}) and highly reactive iron (Fe_{HR}) is commonly used as a proxy to reconstruct redox conditions; a moderate Fe_{Py}/Fe_{HR} ratio (<0.8) is interpreted to indicate 'ferruginous' (Fe-rich) conditions, whereas $Fe_{Py}/Fe_{HR} > 0.8$ indicates euxinia[19]. Ratios of Fe_{Py} to Fe_{HR} calculated by REDBIO are consistent with this concept and with independent iron speciation data from the NAT (Fig. 2j)[12]. They show an oscillation between ferruginous and euxinic states that is maintained by the redox contrast between the NAT and better oxygenated ocean basins such as the Panthalassa Ocean. In most parts of the Panthalassa, primary and EP are limited by iron because the large and strongly ventilated Panthalassa Ocean (Supplementary Fig. 4) receives little iron from land and from seafloor sediments. Phytoplankton in the Panthalassa Ocean depend on dissolved iron to thrive, which is released from sediments in the reducing NAT and transported into the Panthalassa Ocean by ocean currents. Hence, phytoplankton in the Panthalassa flourish when the NAT is enriched in dissolved Fe, but decline when the iron supply is diminished by sulfide precipitation in the NAT. The NAT is in turn oxygenated by currents that originate in the Panthalassa. Low productivity and respiration in the Panthalassa therefore promote the oxygenation of the NAT until the redox state of this reducing ocean basin swings back from euxinic to Fe-rich conditions. The resulting iron fertilization of the Panthalassa leads to a decline in the lateral oxygen supply from this basin to the NAT until the NAT falls back into euxinia. In this way, a redox see-saw is established (Fig. 3), maintaining periodic changes in ocean oxygenation and productivity across the global ocean (Supplementary Figs. 9 and 10).

The cycle length is controlled by concomitant changes in dissolved phosphate, which has an ocean residence time of about 25 kyr in the model ocean. As reactive N is provided by widespread nitrogen fixation[27], the productivity of the Fe-rich NAT is ultimately limited by phosphate (Fig. 2). The global dissolved phosphate inventory is largely controlled by P burial on the broad inner shelves of the NAT and the Tethys that remain oxygenated over the entire redox cycle[22,28]. As the NAT and the Tethys are less productive when intermediate and deep waters are enriched in Fe, rain rates of marine P to the shelf and the resulting shelf P burial fluxes are diminished during these phases (Supplementary Fig. 11). Dissolved phosphate slowly increases when these restricted basins are enriched in Fe because the riverine P input exceeds the P burial flux (Supplementary Fig. 11). The resulting rise in dissolved phosphate promotes EP, P burial, respiration and sulfate reduction in these basins until their redox state descends into euxinia. Under euxinic conditions, dissolved phosphate slowly declines because P burial on the shelf exceeds the riverine flux (Supplementary Fig. 11). The decline in dissolved P and EP continue until the NAT swings back into the Fe-rich state (Fig. 3). The oscillation occurs only over a certain range of riverine P fluxes (Fig. 1). Higher riverine inputs (>125 Gmol yr^{-1}) create permanent euxinia in the poorly ventilated basins, whereas lower fluxes (<107 Gmol yr^{-1}) inhibit the onset of euxinia.

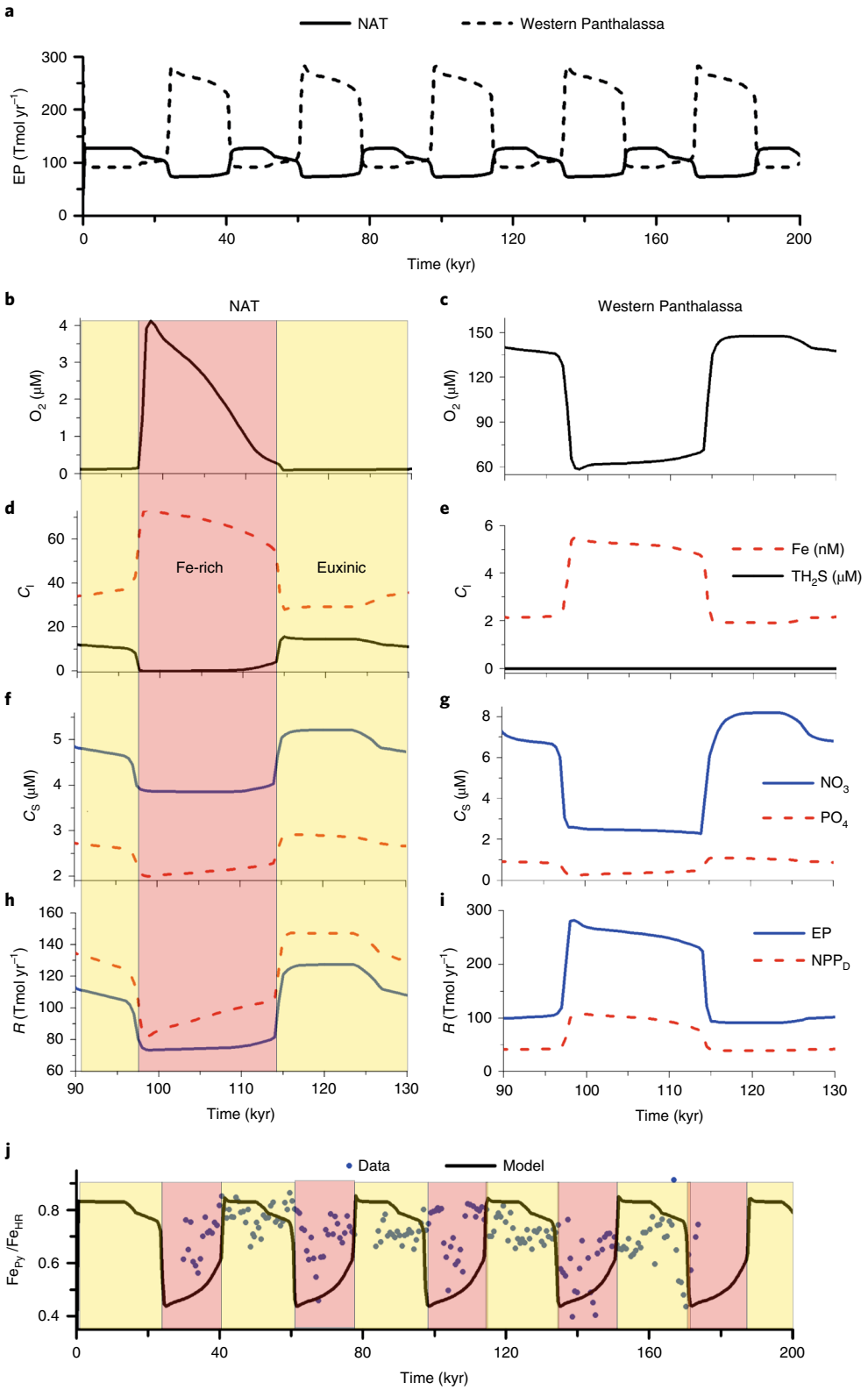

Fig. 2 | REDBIO results for constant P_{CO_2} (500 ppmv) and riverine P flux (116 Gmol yr^{-1}). **a**, EP of POC at 240 m water depth. **b**,**c**, Dissolved oxygen concentration at 240–1,240 m water depth in the NAT (**b**) and the Western Panthalassa (**c**). **d**,**e**, Total dissolved iron ($Fe = Fe^{2+} + Fe^{3+}$) and total dissolved sulfide (TH_2S) in intermediate water (C_I) at 240–1,240 m in the NAT (**d**) and the Western Panthalassa (**e**). **f**,**g**, Dissolved phosphate and nitrate concentrations in surface water (C_S) at 0–240 m water depth in the NAT (**f**) and the Western Panthalassa (**g**). **h**,**i**, Rates (R) of net primary production of POC by diazotrophic phytoplankton (NPP_D) and total EP at 240 m depth in the NAT (**h**) and the Western Panthalassa (**i**). **j**, Ratio of Fe_{Py}/Fe_{HR} in sediments of the NAT deposited at 240–1,240 m water depth. Fe_{Py}/Fe_{HR} data are from the Tarfaya Basin located at the eastern boundary of the NAT[12]. Sediment depths[12] were converted into model time by applying a linear sedimentation rate of 3.0 cm kyr^{-1} (ref. [4]). Euxinic and Fe-rich periods in the NAT are shaded yellow and red, respectively.

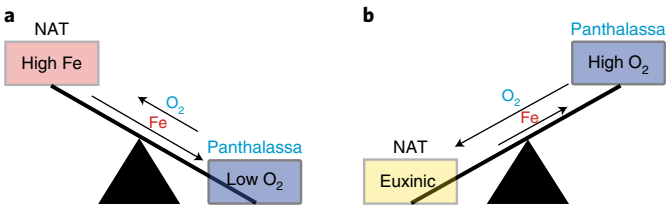

Fig. 3 | The redox see-saw in the mid-Cretaceous ocean. a, The NAT is enriched in dissolved Fe when nitrogen fixation, EP, P burial in shelf sediments and dissimilatory sulfate reduction are limited by low phosphate concentrations. Fe-rich conditions in the NAT induce high iron fluxes into the iron-limited Panthalassa Basin, where dissolved oxygen declines due to the resulting increase in EP and respiration. **b**, The NAT is euxinic when EP and sulfate reduction are promoted by high phosphate concentrations. Iron fluxes from the NAT and respiration in the Panthalassa are diminished when the NAT is euxinic. The lengths of the arrows indicate the fluxes of iron and oxygen. When tipping from **b** to **a**, the NAT is laterally ventilated by oxygen-bearing water masses originating from the Panthalassa. The ventilation increases when the NAT is euxinic due to the reduced iron flux and the resulting oxygen increase in the Panthalassa. The NAT switches from euxinic to Fe-rich conditions because sulfate reduction is suppressed by the enhanced oxygen supply from the Panthalassa and by the enhanced burial of phosphorus in shelf sediments. When tipping from **a** to **b**, the NAT does not remain in the Fe-rich state but falls back into euxinia because Fe-rich conditions in the NAT lead to a decline in the oxygen supply from the Panthalassa and an increase in the phosphate inventory due to the decline in shelf burial.

Interpretation of the ferruginous proxy signature

Our REDBIO model also helps to better understand the nature of the ocean's redox state corresponding to a ferruginous sedimentary proxy signature[12,29–32]. In our modelling scenarios, a ferruginous signature ($Fe_{Py}/Fe_{HR} < 0.8$) corresponds to a water column with elevated dissolved Fe concentrations (up to 0.07 µM). However, this signature does not imply that Fe reduction is the dominant organic carbon respiration pathway[33]. Instead, oxygen and nitrate are the most important electron acceptors under these conditions, whereas sulfate reduction is the dominant process under euxinic conditions, both in the water column and in the sediments (Supplementary Section 3, Supplementary Table. 4). Dissimilatory iron reduction is limited by iron supply—that is, the rain of reactive ferric iron through the water column towards the seabed. Even though the rain rate of particulate ferric iron is enhanced by the iron redox shuttle at the oxic–anoxic interface of the water column, the supply of ferric iron is too low to contribute significantly to organic matter degradation, both under ferruginous and euxinic proxy signatures[18]. Vivianite (iron phosphate) formation and the scavenging of phosphate by ferric iron particles[30,34] have no significant effect on dissolved phosphate due to the moderate dissolved iron concentration in the water column (Fig. 2d, Supplementary Section 4). In REDBIO, Fe-rich conditions develop in a narrow redox window in which dissolved oxygen and nitrate concentrations are high enough to suppress sulfate reduction but too low to remove all iron from the water column, which is constantly replenished by benthic iron release. In this respect, the Fe-rich conditions in our modelling scenarios are similar to the redox state observed in modern oxygen minimum zones[35,36].

Impact of the marine redox see-saw on atmospheric p_{CO_2}

Another simulation was conducted to explore the effect of the redox see-saw on atmospheric p_{CO_2}. The redox-related changes in ocean productivity are strong enough to create p_{CO_2} changes of up to 300 ppm, which significantly affects global climate (Fig. 4). Additional feedbacks arise in these simulations as ocean circulation, sea surface temperatures, weathering rates and riverine P fluxes are governed by atmospheric p_{CO_2}. As a consequence, the cycle length increases from 37 kyr at constant p_{CO_2} (500 ppm) to about 50 kyr for the REDBIO model with dynamic p_{CO_2} (Fig. 4). Owing to p_{CO_2}-driven changes in chemical weathering, the riverine P flux varies dynamically between 113 and 121 Gmol yr^{-1}—close to the prescribed value applied in the previous simulation (116 Gmol yr^{-1}) and within the window where stable oscillations occur (Fig. 1). Atmospheric p_{CO_2} change is induced by the redox-controlled biological pump (EP) transferring CO_2 into the ocean's interior. The increase in global EP induced by Fe-rich conditions in the NAT (Fig. 4) is responsible for the positive correlation between p_{CO_2} and ocean oxygenation (Fig. 4). UVic simulations with a constant P inventory show a negative correlation between these parameters due to the decrease in oxygen solubility in surface waters under high p_{CO_2} (Supplementary Fig. 7). Although changes in solubility and vertical mixing are considered in REDBIO, they are overwhelmed by strong biogeochemical feedbacks related to the dynamic P inventory[22,37]. Hence, the relationship between ocean oxygenation and atmospheric p_{CO_2} is governed by the redox see-saw rather than physical changes in water circulation and temperature. The redox see-saw also produces a negative correlation between the global export and burial of particulate organic carbon (BPOC). Most BPOC takes place on the broad shelves of the anoxic NAT and Tethys basins, whereas global EP is dominated by the better oxygenated ocean basins with narrower continental shelves and hence lower particulate organic carbon (POC) accumulation (Fig. 4).

High-resolution $\delta^{13}C$ records for $CaCO_3$ and POC from the mid-Cretaceous NAT show signatures that are consistent with our model results (Fig. 4h). They feature high $\delta^{13}C$ values in bioturbated, POC-depleted sediments that were probably deposited during non-euxinic phases, and low values in laminated, POC-rich sediments accumulated under euxinic conditions[6,38]. These trends are surprising, because the spread of euxinia in the NAT should lead to a steepening of the vertical $\delta^{13}C$ DIC gradient and an increase in surface water $\delta^{13}C$ DIC, pelagic $\delta^{13}C$ for $CaCO_3$ and POC. However, global EP decreases when the NAT turns euxinic (Fig. 4b) due to the concomitant decrease in dissolved iron concentrations and decline in EP in the Panthalassa Ocean (Fig. 4g). Hence, $\delta^{13}C$ values in the Panthalassa surface ocean are low when the NAT attains a euxinic state (Fig. 4i). The $\delta^{13}C$ records for $CaCO_3$ and POC in the NAT reflect these changes, which are transmitted via rapid horizontal surface water exchange with the adjacent Panthalassa Basin (Supplementary Fig. 13) and are caused by the redox see-saw operating in the mid-Cretaceous ocean.

Response to orbital forcing

Further simulations were conducted to study the response of REDBIO to external orbital forcing when the global riverine P flux is assumed to be modulated by eccentricity (Supplementary Information, Supplementary Figs. 16–18). The power spectra of organic carbon burial rates are very similar to those observed in the NAT[3,10,23] when the global riverine P flux is allowed to change by up to ±13% due to eccentricity forcing (Fig. 5). The wavelengths of major peaks observed in the model results (435 kyr, 94 kyr, 49 kyr, 39 kyr, 21 kyr) largely correspond to those predicted by orbital theory (long eccentricity E1: 405 kyr, short eccentricity E3: 97 kyr, obliquity O1: 49–50 kyr, obliquity O2: 38–39 kyr, precession P1: 22 kyr)[3,23,39,40]. As the model was forced only by eccentricity (Fig. 5), the peaks at shorter wavelengths resembling obliquity and precession signals are not preset by external orbital forcing, but generated by the response of the internal redox see-saw to eccentricity forcing.

Our redox-resolving REDBIO model shows that 37–50 kyr cycles that were previously ascribed to obliquity forcing can be generated

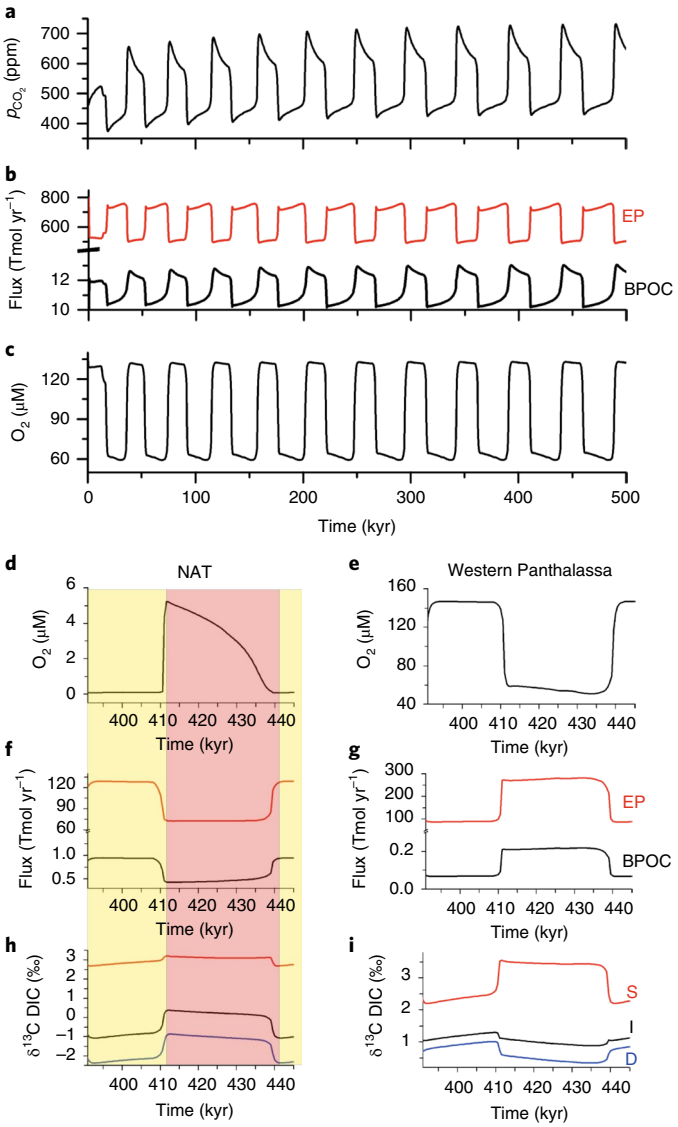

Fig. 4 | REDBIO results for dynamic pCO_2 and riverine P flux. a, p_{CO_2}. **b**, Global EP of POC at 240 m water depth and global rate of BPOC in marine sediments. **c**, Global mean dissolved oxygen concentration. **d**,**e**, Dissolved oxygen concentration at 240–1,240 m water depth in the NAT (**d**) and the Western Panthalassa (**e**). **f**,**g**, EP at 240 m water depth and BPOC in slope sediments at 240–1,240 m water depth in the NAT (**f**) and the Western Panthalassa (**g**). **h**,**i**, δ^{13}C of dissolved inorganic carbon (DIC) at 0–240 m (S), 240–1,240 m (I) and >1,240 water depth (D) in the NAT (**h**) and the Western Panthalassa (**i**). Euxinic and Fe-rich periods in the NAT are shaded yellow and red, respectively.

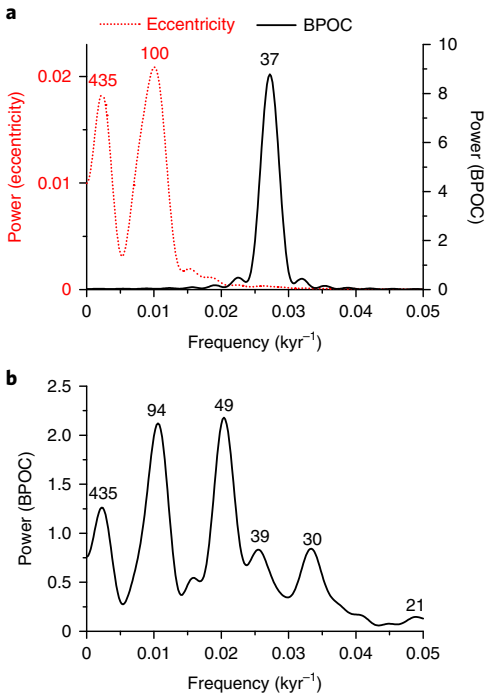

Fig. 5 | Spectral analysis of model results. BPOC on the continental slope of the NAT (240–1,240 m water depth) were calculated and analysed for a REDBIO simulation with constant p_{CO_2}(500 ppmv). **a**, Power spectra of eccentricity (La10a) used as model forcing[39] and the standard model run without orbital forcing (Fig. 2). **b**, Power spectrum for a model run where the global riverine P flux changes by up to ±13% due to eccentricity forcing (Supplementary Section 6). The numbers above the power spectra indicate the wavelengths of major peaks (in kyr). The spectral signature of the model results was analysed using the Blackman–Tukey method and a Bartlett window with a bandwidth of 0.005.

by the internal nonlinear dynamics of the marine biogeochemical system. Our modelling reveals that the enigmatic dominance of this signal over the Cretaceous Thermal Maximum is probably caused by marine redox feedbacks that induce regular oscillations between ferruginous and euxinic conditions in major ocean basins and drive periodic changes in atmospheric p_{CO_2}. This marine redox see-saw may also have been active during other geological periods as ferruginous/euxinic proxy signatures have been documented in geological records that cover large parts of Earth's history[19,29,31]. Our findings support results of previous modelling studies showing that biogeochemical feedbacks may generate oscillations in carbon cycling and global climate[41–43], and confirm that an improved understanding of the nonlinear response of the Earth system to external forcing is required to unravel the geological record.

Online content

Any methods, additional references, Nature Research reporting summaries, source data, statements of code and data availability and associated accession codes are available at https://doi.org/10.1038/s41561-019-0359-x.

Received: 20 July 2018; Accepted: 29 March 2019;
Published online: 13 May 2019

References

1. Friedrich, O., Norris, R. D. & Erbacher, J. Evolution of middle to Late Cretaceous oceans—a 55 m.y. record of Earth's temperature and carbon cycle. *Geology* **40**, 107–110 (2012).
2. O'Brien, C. L. et al. Cretaceous sea-surface temperature evolution: constraints from TEX_{86} and planktonic foraminiferal oxygen isotopes. *Earth Sci. Rev.* **172**, 224–247 (2017).
3. Meyers, S. R., Sageman, B. B. & Arthur, M. A. Obliquity forcing of organic matter accumulation during Oceanic Anoxic Event 2. *Paleoceanography* **27**, PA3212 (2012).
4. Kolonic, S. et al. Black shale deposition on the northwest African Shelf during the Cenomanian/Turonian oceanic anoxic event: climate coupling and global organic carbon burial. *Paleoceanography* **20**, PA1006 (2005).
5. Kuhnt, W., Luderer, F., Nederbragt, S., Thurow, J. & Wagner, T. Orbital-scale record of the late Cenomanian–Turonian oceanic anoxic event (OAE-2) in the Tarfaya Basin (Morocco). *Int. J. Earth. Sci.* **94**, 147–159 (2005).
6. Kuhnt, W. et al. Unraveling the onset of Cretaceous Oceanic Anoxic Event 2 in an extended sediment archive from the Tarfaya-Laayoune Basin, Morocco. *Paleoceanography* **32**, 923–946 (2017).

7. Sageman, B. B., Rich, J., Arthur, M. A., Birchfield, G. E. & Dean, W. E. Evidence for Milankovitch periodicities in Cenomanian–Turonian lithologic and geochemical cycles, western interior USA. *J. Sediment. Res.* **67**, 286–302 (1997).
8. Eldrett, J. S. et al. Origin of limestone-marlstone cycles: astronomic forcing of organic-rich sedimentary rocks from the Cenomanian to early Coniacian of the Cretaceous Western Interior Seaway, USA. *Earth Planet. Sci. Lett.* **423**, 98–113 (2015).
9. Bosmans, J. H. C., Hilgen, F. J., Tuenter, E. & Lourens, L. J. Obliquity forcing of low-latitude climate. *Clim. Past* **11**, 1335–1346 (2015).
10. Kuhnt, W., Nederbragt, A. & Leine, L. Cyclicity of Cenomanian-Turonian organic-carbon-rich sediments in the Tarfaya Atlantic Coastal Basin (Morocco). *Cretaceous Res.* **18**, 587–601 (1997).
11. Wagner, T., Hofmann, P. & Flögel, S. Marine black shale deposition and Hadley Cell dynamics: a conceptual framework for the Cretaceous Atlantic Ocean. *Mar. Petrol. Geol.* **43**, 222–238 (2013).
12. Poulton, S. W. et al. A continental-weathering control on orbitally driven redox-nutrient cycling during Cretaceous Oceanic Anoxic Event 2. *Geology* **43**, 963–966 (2015).
13. Flögel, S., Wallmann, K. & Kuhnt, W. Cool episodes in the Cretaceous—exploring the effects of physical forcings on Antarctic snow accumulation. *Earth Planet. Sci. Lett.* **307**, 279–288 (2011).
14. Laurin, J., Meyers, S. R., Ulicny, D., Jarvis, I. & Sageman, B. B. Axial obliquity control on the greenhouse carbon budget through middle- to high-latitude reservoirs. *Paleoceanography* **30**, 133–149 (2015).
15. Bohlen, L., Dale, A. & Wallmann, K. Simple transfer functions for calculating benthic fixed nitrogen losses and C:N:P regeneration ratios in global biogeochemical models. *Glob. Biogeochem. Cycles* **26**, GB3029 (2012).
16. Van Cappellen, P. & Ingall, E. D. Benthic phosphorus regeneration, net primary production, and ocean anoxia: a model of the coupled marine biogeochemical cycles of carbon and phosphorus. *Paleoceanography* **9**, 677–692 (1994).
17. Wallmann, K. Phosphorus imbalance in the global ocean? *Glob. Biogeochem. Cycles* **24**, GB4030 (2010).
18. Dale, A. W. et al. A revised global estimate of dissolved iron fluxes from marine sediments. *Glob. Biogeochem. Cycles* **29**, 691–707 (2015).
19. Raiswell, R. & Canfield, D. E. The iron biogeochemical cycle past and present. *Geochem. Perspect.* **1**, 1–220 (2012).
20. Scholz, F., McManus, J., Mix, A. C., Hensen, C. & Schneider, R. R. The impact of ocean deoxygenation on iron release from continental margin sediments. *Nat. Geosci.* **7**, 433–437 (2014).
21. Monteiro, F. M., Pancost, R. D., Ridgwell, A. & Donnadieu, Y. Nutrients as the dominant control on the spread of anoxia and euxinia across the Cenomanian-Turonian oceanic anoxic event (OAE2): model-data comparison. *Paleoceanography* **27**, PA4209 (2012).
22. Ruvalcaba Baroni, I., Topper, R. P. M., van Helmond, N., Brinkhuis, H. & Slomp, C. P. Biogeochemistry of the North Atlantic during oceanic anoxic event 2: role of changes in ocean circulation and phosphorus input. *Biogeosciences* **11**, 977–993 (2014).
23. Beil, S. et al. New insights into Cenomanian paleoceanography and climate evolution from the Tarfaya Basin, southern Morocco. *Cretaceous Res.* **84**, 451–473 (2018).
24. Ruttenberg, K. C. Reassessment of the oceanic residence time of phosphorus. *Chem. Geol.* **107**, 405–409 (1993).
25. Flögel, S. et al. Simulating the biogeochemical effects of volcanic CO_2 degassing on the oxygen-state of the deep ocean during the Cenomanian/Turonian Anoxic Event (OAE2). *Earth Planet. Sci. Lett.* **305**, 371–384 (2011).
26. Meyer, K. M. & Kump, L. R. Oceanic euxinia in Earth history: causes and consequences. *Annu. Rev. Earth Planet. Sci.* **36**, 251–288 (2008).
27. Kuypers, M. M. M., van Breugel, Y., Schouten, S., Erba, E. & Damste, J. S. S. N_2-fixing cyanobacteria supplied nutrient N for Cretaceous oceanic anoxic events. *Geology* **32**, 853–856 (2004).
28. Lenton, T. M. & Daines, S. J. The effects of marine eukaryote evolution on phosphorus, carbon and oxygen cycling across the Proterozoic–Phanerozoic transition. *Emerg. Topics Life Sci.* **2**, 267–278 (2018).
29. Poulton, S. W. & Canfield, D. E. Ferruginous conditions: a dominant feature of the ocean through Earth's history. *Elements* **7**, 107–112 (2011).
30. März, C. et al. Redox sensitivity of P cycling during marine black shale formation: dynamics of sulfidic and anoxic, non-sulfidic bottom waters. *Geochim. Cosmochim. Acta* **72**, 3703–3717 (2008).
31. Clarkson, M. O. et al. Dynamic anoxic ferruginous conditions during the end-Permian mass extinction and recovery. *Nat. Commun.* **7**, 12236 (2016).
32. Dickson, A. J. et al. The spread of marine anoxia on the northern Tethys margin during the Paleocene-Eocene Thermal Maximum. *Paleoceanography* **29**, 471–488 (2014).
33. Lenton, T. M. & Daines, S. J. Biogeochemical transformations in the history of the ocean. *Annu. Rev. Mar. Sci.* **9**, 31–58 (2017).
34. Dellwig, O. et al. A new particulate Mn–Fe–P-shuttle at the redoxcline of anoxic basins. *Geochim. Cosmochim. Acta* **74**, 7100–7115 (2010).
35. Scholz, F. et al. Nitrate-dependent iron oxidation limits iron transport in anoxic ocean regions. *Earth Planet. Sci. Lett.* **454**, 272–281 (2016).
36. Scholz, F. Identifying oxygen minimum zone-type biogeochemical cycling in Earth history using inorganic geochemical proxies. *Earth Sci. Rev.* **184**, 29–45 (2018).
37. Tsandev, I. & Slomp, C. P. Modeling phosphorous cycling and carbon burial during Cretacious Oceanic Anoxic Events. *Earth Planet. Sci. Lett.* **286**, 71–79 (2009).
38. Kuypers, M. M. M. et al. Orbital forcing of organic carbon burial in the proto-North Atlantic during oceanic anoxic event 2. *Earth Planet. Sci. Lett.* **228**, 465–482 (2004).
39. Laskar, J., Fienga, A., Gastineau, M. & Manche, H. La2010: a new orbital solution for the long-term motion of the Earth. *Astron. Astrophys.* **532**, A89 (2011).
40. Berger, A., Loutre, M. F. & Laskar, J. Stability of the astronomical frequencies over the Earth's history for paleoclimate studies. *Science* **255**, 560–566 (1992).
41. Handoh, I. C. & Lenton, T. M. Periodic mid-Cretaceous oceanic anoxic events linked by oscillations of the phosphorus and oxygen biogeochemical cycles. *Glob. Biogeochem. Cycles* **17**, 1092 (2003).
42. Saltzman, B. & Maasch, D. K. Carbon cycle instability as a cause of the late Pleistocene ice age oscillations: modeling the asymmetric response. *Glob. Biogeochem. Cycles* **2**, 177–185 (1988).
43. Wallmann, K. Is late Quaternary climate change governed by self-sustained oscillations in atmospheric CO_2? *Geochim. Cosmochim. Acta* **132**, 413–439 (2014).

Acknowledgements

This study was supported by the German Research Foundation via Collaborative Research Center 754 (Climate–Biogeochemistry Interactions in the Tropical Ocean, SFB 754) and the Emmy Noether Program (independent junior research group ICONOX). Further support was provided by the Helmholtz Association via the ESM project.

Author contributions

K.W. designed REDBIO and wrote the manuscript. S.F., S.S. and T.P.K. set up the UVic Earth System Model with the mid-Cretaceous continent configuration. F.S. contributed to the discussion of biogeochemical cycling in anoxic oceans. A.W.D supported the development of REDBIO. W.K. helped in the interpretation of the mid-Cretaceous geological record and the spectral analysis of model results.

Competing interests

The authors declare no competing interests.

Additional information

Supplementary information is available for this paper at https://doi.org/10.1038/s41561-019-0359-x.

Reprints and permissions information is available at www.nature.com/reprints.

Correspondence and requests for materials should be addressed to K.W.

Publisher's note: Springer Nature remains neutral with regard to jurisdictional claims in published maps and institutional affiliations.

Methods

A Cretaceous UVic Earth System Climate Model was set up to simulate the distribution of dissolved oxygen in the global ocean over a range of p_{CO_2} values (500, 1,200, 1,800 and 2,400 ppm) assuming constant phosphate and alkalinity inventories. The model was run over a period of 8 kyr for each p_{CO_2} value to reach a steady state. The model consists of an ocean general circulation model (Modular Ocean Model, Version 2) with a nutrient–phytoplankton–zooplankton–detritus model[44] coupled to a vertically integrated two-dimensional energy–moisture balance model of the atmosphere, a dynamic–thermodynamic sea-ice model, a dynamic global land and vegetation model and a $CaCO_3$ sediment model[45,46]. The model is driven by seasonal variations in solar insolation at the top of the atmosphere and seasonally varying wind stress and wind fields for each p_{CO_2} value[47]. The coupled model has a 1.8°×1.8° horizontal resolution and conserves energy, water and carbon without the use of flux adjustment[48]. A comprehensive description of the Cretaceous UVic configuration is included in the Supplementary Section 1.

The Cretaceous ocean was separated into 12 basins to allow integration over longer timescales (Supplementary Fig. 8). Surface water (0–240 m), intermediate water (240–1,240 m) and deep water boxes (>1,240 m) were defined for each of these basins. Surface temperatures, volumes, seafloor areas and bidirectional water fluxes across each interface of the 36 ocean boxes were defined using output from the steady-state UVic simulations. Water fluxes and temperatures were calculated as function of atmospheric p_{CO_2} using a linear interpolation of UVic outputs (annual means). REDBIO was embedded in this fully dynamic ocean box model. It considers that global inventories of all dissolved tracers (oxygen, nitrate, ammonium, phosphate, ferric iron, ferrous iron, total dissolved sulfide, dissolved inorganic carbon (^{12}C and ^{13}C) and total alkalinity) change over time due to weathering inputs from land, CO_2 and O_2 fluxes across the ocean–atmosphere interface, nitrogen fixation, denitrification and redox-dependent fluxes at the seabed. Feedbacks between ocean productivity, respiration, benthic fluxes and nutrient contents create internal oscillations with cycle lengths of about 37–50 kyr. This nonlinear behaviour arises because nutrient contents (phosphate, nitrate, ammonium and dissolved iron) depend on the oxygenation of intermediate and deep waters, whereas oxygenation is itself a function of nutrient abundance that controls ocean productivity and respiration. Sensitivity tests showed that the oscillations are a robust feature of the model that persists over a significant range of riverine P fluxes (Fig. 1), ventilation rates and kinetic parameter values (Supplementary Section 5). Continental weathering and degassing fluxes, surface temperatures and atmospheric p_{CO_2} were simulated using GEOCARB process formulations[49,50] whereas marine $\delta^{13}C$ values were calculated as described in a previous box model[51]. A detailed description of the REDBIO model is included in the Supplementary Section 2.

Data availability

The authors declare that the data supporting the findings of this study are available within the Article and its Supplementary Information.

Code availability

The UVic model and the REDBIO box model (written in MATHEMATICA) are available from S.F. (sfloegel@geomar.de) and K.W., respectively.

References

44. Keller, D. P., Oschlies, A. & Eby, M. A new marine ecosystem model for the University of Victoria Earth System Climate Model. *Geosci. Model Dev.* **5**, 1195–1220 (2012).
45. Archer, D. A data-driven model of the global calcite lysocline. *Glob. Biogeochem. Cycles* **10**, 511–526 (1996).
46. Weaver, A. J. et al. The UVic Earth System Climate Model: model description, climatology, and applications to past, present and future climates. *Atmos. Ocean* **39**, 361–428 (2001).
47. Flögel, S., Hay, W. W., DeConto, R. M. & Balukhovsk, A. N. Formation of sedimentary bedding couplets in the Western Interior Seaway of North America—implications from climate system modeling. *Palaeogeogr. Palaeoclimatol. Palaeoecol.* **218**, 125–143 (2005).
48. Meissner, K. J., McNeil, B. I., Eby, M. & Wiebe, E. C. The importance of the terrestrial weathering feedback for multimillennial coral reef habitat recovery. *Glob. Biogeochem. Cycles* **26**, GB3017 (2012).
49. Berner, R. A. & Kothavala, Z. GEOCARB III: a revised model of atmospheric CO_2 over Phanerozoic time. *Am. J. Sci.* **301**, 182–204 (2001).
50. Royer, D. L., Donnadieu, Y., Park, J., Kowalczyk, J. & Godderis, Y. Error analysis of CO_2 and O_2 estimates from the long-term geochemical model GEOCARBSULF. *Am. J. Sci.* **314**, 1259–1283 (2014).
51. Wallmann, K., Schneider, B. & Sarnthein, M. Effects of eustatic sea-level change, ocean dynamics, and nutrient utilization on atmospheric pCO_2 and seawater composition over the last 130,000 years. *Clim. Past* **12**, 339–375(2016).